

# Effect of travel speed and sub- $\beta$ transus post deposition heat treatments on thin Ti-6Al-4V laser wire deposits

N. Chekir<sup>a</sup>, Y. Tian<sup>a</sup>, J.J. Sixsmith<sup>b</sup>, M. Brochu<sup>a,\*</sup>

<sup>a</sup> Department of Mining and Materials Engineering, McGill University, Montreal, Quebec, Canada H3A 0C5

<sup>b</sup> Liburdi Automation Inc., Dundas, Ontario, Canada L9H 7K4

## ARTICLE INFO

### Keywords:

Additive manufacturing  
Ti-6Al-4V  
Travel speed  
Heat treatment  
Microstructure characterization  
Mechanical properties

## ABSTRACT

Annealing or HIP below the  $\beta$  transus temperature was found to coarsen the as-built developed microstructure while preserving the developed macro morphology of Laser Wire Deposition (LWD) buildups. Following these thermal cycles, a general decrease in strength along with an increase in elongation have been observed. However, no trends in the tensile results could be extracted due to the scattering of the results. An additional aging cycle substantially stabilized the developed results. Samples processed at 1.4 mm/s exhibited low strength hardly meeting any of the ASTM and AMS minimum requirements and a strong anisotropy in elongation with lower values when tested along the Z direction. Samples processed at 7.2 mm/s exhibited good strength meeting the minimum wrought requirements as set by AMS4911 while elongation showed an isotropic behavior. Hardness has been found to be mostly independent of the experienced sub- $\beta$  transus post deposition heat treatment. Moreover, the grain boundary strengthening mechanism with regards to the  $\alpha$  platelets thicknesses was found to be travel speed dependent.

## 1. Introduction

Ti-6Al-4V is an extremely attractive alloy for structural applications when temperatures do not exceed 600 °C mainly due to its excellent strength to weight ratio and high corrosion resistance [1]. However, high manufacturing costs makes it mostly a niche product to the aerospace and biomedical industries [2–5]. Producing near-net-shape parts using additive manufacturing processes such as Laser Wire Deposition (LWD) processes might in turn reduce the overall production cost of Ti-6Al-4V parts. But variability in generated material properties mainly induced by the choice of deposition parameters and post deposition processes still prevents the use of additive manufacturing as a reliable manufacturing process [6–13].

Annealing processes closer to the  $\beta$  transus temperature yield to a coarser microstructure. They may be associated with the development of grain boundary allotriomorphs  $\alpha_{GB}$  and  $\alpha$  colonies known to be detrimental for the mechanical properties [7,14–16]. Sub-transus thermal are known to preserve macro morphology of the prior  $\beta$  grains [17]. Similar anisotropy in properties to the as-built and stress relieved (SR) samples is typically reported associated to a lower elongation and higher strength when tested along the travel direction commonly named the X direction [15,17,18]. Moreover, coarsening of  $\alpha$  platelets is associated with the drop in strength values and increase in

elongation. Super-transus thermal cycles are associated with an important coarsening of  $\alpha$  platelets but also with the recrystallization of prior  $\beta$  grains into horizontal [15] or equiaxed [7,14] prior  $\beta$  grains. These major structural changes are associated with not only poor strength but also poor elongation [14,15]. Both thermal cycles are characterized by an equivalent or a small drop in hardness measurements when compared to the as-built condition [7,17,18].

In this study, two different travel speeds and four different sub- $\beta$  transus post deposition heat treatments are investigated. The focus behind these different conditions being to produce optimum materials properties. First generated macrostructures and microstructures will be discussed. Then, the effect of the four different thermal cycles on the generated tensile properties including fracture behaviors will be presented for both travel speeds. Finally, a discussion on the strengthening mechanism will be addressed.

## 2. Experimental methods

A Liburdi LAWS 1000 automated deposition system was used to process all samples. This system is equipped with an IPG Yb:YAG fiber laser reaching up to 1 kW power that is focused to fuse the grade 23 Ti-6Al-4V wire (Lancaster Alloys Company Inc.). All deposits were manufactured in an argon inert environment with oxygen levels below

\* Corresponding author.

E-mail address: [mathieu.brochu@mcgill.ca](mailto:mathieu.brochu@mcgill.ca) (M. Brochu).

60 ppm.

Wrought Ti-6Al-4V plates are used as substrates. Two travel speeds are used in this study: 1.4 mm/s and 7.2 mm/s. Single bead characterized by a thickness of 2.5 mm walls were produced. Ratio of wire feed speed over travel speed was kept constant and yielding to a vertical increment of 0.660 mm between each deposited bead. Geometry of the deposited samples accommodated the extraction of tensile specimens as described below.

Macrostructure, microstructure and fractographs were observed using a Nikon light optical microscope equipped with a Clemex vision system and a Hitachi SU-3500 cold field FE-SEM. Structural investigation was done in a plane containing both the travel and buildup directions. These samples were ground up to 1200 SiC grit, followed by polishing with 3 μm and 1 μm diamond suspension and a finish with 0.05 μm colloidal silica. Grinding and polishing were done using a Buhler Ecomet-3 autopolisher equipped with an Automet-2 head. A Kroll's Reagent etchant with 91% deionized water (H<sub>2</sub>O), 6% nitric acid (HNO<sub>3</sub>) and 3% hydrofluoric acid (HF) was then used on the mounted samples to reveal the structural features using the optical microscope.

Samples were heat-treated post deposition following an annealing heat treatment according to AMS2801 or a HIP process following AMS4999. These two cycles were attempted to remove the effect of deposition parameters and homogenizing the microstructure. Furnace cooling followed all the previous heat treatments. The effect of an aging was also studied according to AMS2801 standard, as a strengthening process following the two previous heat treatments. Only cooling rate of the annealing heat treatment was changed to argon quench prior the aging treatment. Aging soaking temperature following the HIP process was reached by furnace cooling from the HIP temperature. Table 1 summarizes the heat treatments and the according abbreviations used in this research.

The Vickers hardness was measured by means of a Clark Microhardness (CM-100AT) indenter, using a 100 g load. A minimum of 25 measurements was done along the build direction for each of the reported values.

Machined subsize specimens meeting ASTM E8 requirements with a thickness of 1.4 mm, a gage width of 6.35 mm and a gage length of 25.4 mm have been extracted for all the heat-treated conditions. Numbers of samples tested in each condition are summarized in Table 2. Samples were tested at room temperature with a crosshead speed of 2.54 mm/min until fracture using a United SFM-20 kN load frame equipped with a calibrated load cell and an extensometer. Finally, average values of wrought tensile properties produced from five specimens extracted from the base plate and reproducing the subsize specimens geometry previously described have been used to normalize all the results.

### 3. Results and discussion

#### 3.1. Structure evaluation

Each of the thermal cycles steps in this section resulted in fairly similar results and will be described only by some representative micrographs in Fig. 1. An annealing or a HIP process removes the visual

**Table 1**  
Selected heat treatments.

Heat Treatment	Specification	Cooling Rate	Abbreviation
Annealing	AMS2801	Furnace cooling	A
Hot isostatic pressure	AMS4999	Furnace cooling	HIP
Annealing followed by aging	AMS2801	Argon quench	AA
	AMS2801	Furnace cooling	
Hot isostatic pressure followed by aging	AMS4999	Furnace cooling to aging temperature	HIPA
	AMS2801	Furnace cooling	

**Table 2**

Number of static tensile samples tested per condition.

Travel Speed:	1.4 mm/s		7.2 mm/s	
	X	Z	X	Z
A	3	5	4	5
HIP	3	5	4	5
AA	3	5	4	5
HIPA	3	5	4	5

banding phenomenon that was described in a previous study [19] and induced by the deposition of additional beads as shown in Figs. 1a) and 1b). Since complete dissolution of the α phase within the β phase did not occur, morphology of previously developed prior β grains at both travel speeds remained fairly unchanged including the horizontal prior β grains that developed for the samples processed at 1.4 mm/s [19].

Regarding the microstructure, an important coarsening of the α platelets has been observed for both the annealing and the HIP processes followed or not by aging as shown in Table 3. α platelets thicknesses remained statistically similar for all the different conditions. Morphology of the alpha platelets including colonies and α<sub>GB</sub> and described in more details in a previous study [19] were mostly preserved when present in the as-built microstructure. The coarsening phenomenon in Ti-6Al-4V is usually explained by means of Ostwald ripening and termination migration that ends up with a smaller aspect ratio but thicker platelets [20–22]. Coarsening kinetics can be interpreted by the classical LSW theory developed by Lifshitz, Slyozov and Wagner. It provides a relationship linking the average α platelet thickness to the heat treatment soaking time as follow:

$$d = (K_{LSW} t)^n \quad (1)$$

Where  $d$  is the mean α thickness,  $t$  the heat treatment soaking time,  $n$  the coarsening coefficient and  $K_{LSW}$  a constant coarsening coefficient during the heat treatment defined as:

$$K_{LSW} = \frac{8D\gamma C_\beta^\alpha V_m}{9RT} \quad (2)$$

Where  $D$  is the solute diffusion coefficient through the β phase,  $\gamma$  is the α/β interface energy,  $C_\beta^\alpha = C_\beta(1-C_\beta)/(C_\alpha - C_\beta)^2$  with  $C_\beta$  the solute equilibrium concentration in the β phase and  $C_\alpha$  the solute equilibrium concentration in the α phase [20,22],  $V_m$  is the molar volume of the α phase,  $R$  is the gas constant and  $T$  the absolute temperature. Finally, by taking into consideration the initial mean α thickness  $d_0$ , Eq. (1) becomes:

$$d^{1/n} - d_0^{1/n} = K_{LSW} t \quad (3)$$

The main difference between the annealing heat treatments at the both travel speed samples resides in the initial condition. Indeed, from Eq. (3), the greater coarsening in average for samples built at 1.4 mm/s and following the annealing process can be explained by the fact that initial structure in the as built (AB) condition was already coarser than the one developed at 7.2 mm [19]. Smaller soaking time of 15 min can also be accounted as one of the reasons restricting the amount of coarsening. HIP soaking time of 2 h seems to allow the structure to reach an optimum α platelet distribution coarser than the one developed by annealing. It can be assumed moreover that for the same temperature as the one used in annealing, pressure will also likely affect the  $C_\beta^\alpha$  term.

Prior to the aging thermal cycle, α platelets are not well defined in the micrographs shown in Figs. 1c) and 1d) and pointed out for some of them by red arrows. A metastable state following furnace cooling seems to have been reached by combining together some of the α platelets and most probably dictated by an incomplete Ostwald ripening behavior.

Precipitation of the β phase occurred following the aging cycle. Preferential sites for the precipitation of the β phase exist at the

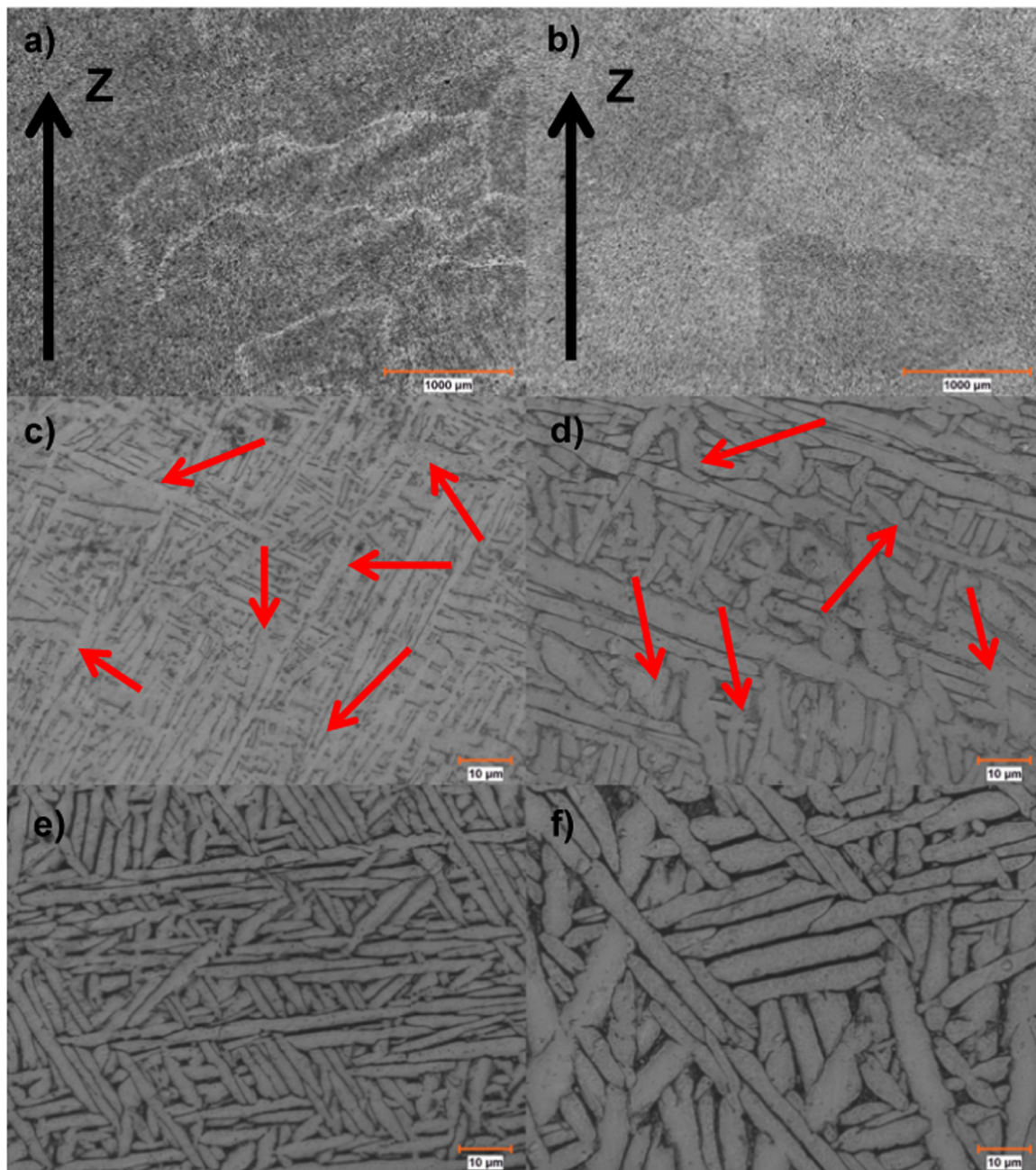


Fig. 1. Macrostructures a) at 1.4 mm/s in the annealed condition and b) at 7.2 mm/s in the HIPed condition. Microstructures c) at 7.2 mm/s in the annealed condition, d) at 1.4 mm/s in the HIPed condition, e) at 1.4 mm/s in the annealed and aged condition and f) at 7.2 mm/s in the HIPed and aged condition.

Table 3  
Alpha platelets thicknesses.

Thermal cycle	Travel speed	
	1.4 mm/s	7.2 mm/s
A	1928 nm ± 420 nm	1447 nm ± 324 nm
HIP	2280 nm ± 565 nm	2288 nm ± 518 nm
AA	2178 nm ± 400 nm	1939 nm ± 442 nm
HIPA	2960 nm ± 736 nm	1955 nm ± 458 nm

connection of two or more platelets that underwent incomplete Ostwald ripening behavior and not only at the  $\alpha$  platelets tips [19]. As a result, clear  $\alpha$  platelets can be observed with the optical microscope as shown in Figs. 1e) and 1f). Signs of diffusional partitioning have also been

observed: Secondary  $\alpha$  platelets precipitated forming a very fine  $\alpha + \beta$  basket weave arrangement comprised in between original  $\alpha + \beta$  basket weave arrangements. This phenomenon has previously been reported by Baufeld et al. [18] in the AB condition and is associated with the heat treatment in the  $\alpha/\beta$  phase field induced by the deposition of additional layers.

### 3.2. Tensile properties

#### 3.2.1. Annealed or HIPed static tensile properties

Post deposition annealing or HIP cycles below the  $\beta$  transus temperature were attempted in order to try to remove the effect of deposition parameters on the developed microstructure. The idea behind the HIP process was mainly to see if undetected structural defects such as micro pores or lack of fusion would affect the final tensile properties.

**Table 4**  
Room temperature static tensile properties of the annealed or HIPed specimens.

Travel Speed (mm/s)	Heat Treatment	Tensile Direction	Yield Strength ((MPa/MPa)*100)	Ultimate Tensile Strength ((MPa/MPa)*100)	Elongation ((%/%)*100)	Reduction of Area (%)
1.4	A	X	67.5 < <b>75.9</b> < 80.2, 5.9	71.0 < <b>78.8</b> < 82.7, 5.5	71 < <b>79</b> < 94, 10	26.9 < <b>39.5</b> < 52.1, 17.8
		Z	71.9 < <b>72.2</b> < 72.9, 0.4	74.4 < <b>75.0</b> < 76.3, 0.7	46 < <b>66</b> < 82, 14	27.5 < <b>33.1</b> < 45.2, 8.2
	HIP	X	79.3 < <b>81.1</b> < 83.4, 1.7	82.9 < <b>84.3</b> < 86.5, 1.5	29 < <b>43</b> < 64, 15	10.6 < <b>18.0</b> < 25.4, 10.5
		Z	73.3 < <b>74.3</b> < 76.2, 1.0	75.1 < <b>77.8</b> < 80.5, 1.8	40 < <b>81</b> < 114, 26	9.3 < <b>28.8</b> < 45.2, 18.2
7.2	A	X	74.3 < <b>74.6</b> < 75.7, 0.6	75.7 < <b>76.3</b> < 76.9, 0.4	56 < <b>69</b> < 80, 10	31.6 < <b>42.2</b> < 54.2, 11.4
		Z	83.4 < <b>85.9</b> < 90.2, 2.4	87.8 < <b>90.6</b> < 93.3, 1.8	87.8 < <b>90.6</b> < 93.3, 1.8	26.5 < <b>32.0</b> < 35.9, 6.1
	HIP	X	83.0 < <b>86.2</b> < 88.4, 1.7	86.2 < <b>87.0</b> < 88.2, 0.8	86.2 < <b>87.0</b> < 88.2, 0.8	14.0 < <b>34.7</b> < 51.3, 19.0
		Z	85.3 < <b>87.5</b> < 91.3, 2.0	89.5 < <b>91.1</b> < 93.0, 1.3	89.5 < <b>91.1</b> < 93.0, 1.3	16.1 < <b>32.7</b> < 46.8, 12.8

Results are presented as:  $\sigma_{min} < \bar{\sigma} < \sigma_{max}, SD$  where  $\sigma_{min}$  is the lowest value,  $\bar{\sigma}$  the mean value,  $\sigma_{max}$  the highest value and  $SD$  the standard deviation from the mean value.

Static tensile properties are summarized in Table 4 for these post deposition heat treatments. A general drop in strength was experienced by all the samples when compared with the SR condition [19]. Strength hardly meets the minimum requirements set for cast materials as per ASTM F1108 for samples processed at 1.4 mm/s and the minimum wrought requirements as per AMS4911 for samples processed at 7.2 mm/s. However, no clear trends in strength nor elongation can be extracted from Table 4 due to the scattering of the results in average but also when taking into account the standard deviations. One potential reason for this scattering in the generated results can be associated with the incomplete Ostwald ripening phenomenon of the  $\alpha$  platelets observed in Section 3.1. This is believed to induce an anisotropy in the  $\alpha$  platelets arrangements increasing the maximum slip length of the tested specimens or activating different slip systems during tensile testing reducing in turn the tensile strength of the material and increasing the discrepancy in the results. Coarsening of the microstructure helped though in improving the ductility of the material [5,23]. This is in good agreement with the reported effect of similar heat treatments on the elongation of printed components [15,17,18]. Moreover, generated results in the annealed condition or HIPed condition for both travel speeds are mostly equivalent. As a consequence, a HIP thermal cycle did not improve the tensile properties of the printed components when compared with the tensile results in the annealed condition, confirming eventually the good structural integrity of the parts.

3.2.2. Annealed or HIPed followed by aging static tensile properties

Tensile results generated by an aging cycle following the annealing or HIP cycles are summarized in Table 5. The aging cycle substantially reduced the scattering of the results by precipitating secondary  $\alpha$  platelets as shown in Section 3.1. The drop in strength for both travel speeds observed in the previous section is still experienced in this section. As a consequence, none of the results at 1.4 mm/s met the typical minimum strength requirements set by the AMS and ASTM international standards. As opposed to the samples processed at 7.2 mm/s for which most of the conditions exceeded in average, or in absolute for

the ultimate tensile strength, the minimum wrought requirements set by the AMS4911 specification. Major trends in elongation observed for the SR condition are still present in this section as shown in Table 5. A strong anisotropy in elongation has been observed for the samples produced at 1.4 mm/s with a lower elongation generated for the samples tested along the Z direction and again at the opposite of the typical reported anisotropy [10,17,18,24–26]. In this case, elongation exceeds or hardly meets the minimum requirements as set by the DED specification for the annealed and aged condition tested along the Z direction. As opposed to the samples built at 7.2 mm/s for which elongation consistently exceeds minimum wrought requirements. Eventually, whether samples were produced at 1.4 mm/s or 7.2 mm/s, similar static tensile results were produced following an annealing and aging process or a HIP and aging process. As a consequence, there is no clear advantage again in running a HIP post deposition heat treatment in order to improve the static tensile properties of the samples produced by LWD process used in this study. In addition, substantially different static tensile results were generated for samples built at 1.4 mm/s or 7.2 mm/s, stressing on the importance of selecting optimum deposition parameters at the start of the build.

When comparing these results to typical data generated in the literature as shown in Fig. 2, generated strength at 7.2 mm/s remain above the typical values reported for both LWD [7,14,17,27] and Shape Metal Deposition (SMD) [17] but below average results generated by Laser Powder Deposition (LPD) processes [15,28–31]. However, most of the strengths associated with the samples produced at 1.4 mm/s remain in the lower section of the reported values for LWD and SMD. While most of the reported elongations following these typical heat treatments fall within the same range as all the reported DED processes as seen in Fig. 2b).

Scattering of the results in terms of elongation depicted in Fig. 2b) shows that no clear strength to elongation trend can be derived for any of the processes presented within this paper. Many reasons can explain this last observation. Sample geometry first can influence the generated elongation. ASTM E8 recommends comparing results for samples

**Table 5**  
Room temperature static tensile properties of the annealed or HIPed followed by an aging cycle specimens.

Travel Speed (mm/s)	Heat Treatment	Tensile Direction	Yield Strength ((MPa/MPa)*100)	Ultimate Tensile Strength ((MPa/MPa)*100)	Elongation ((%/%)*100)	Reduction of Area (%)
1.4	AA	X	75.1 < <b>76.4</b> < 77.6, 1.0	78.6 < <b>80.9</b> < 83.0, 1.8	58 < <b>68</b> < 81, 10	19.3 < <b>24.1</b> < 28.9, 6.8
		Z	74.0 < <b>76.0</b> < 77.6, 1.4	75.7 < <b>77.7</b> < 78.0, 1.0	29 < <b>41</b> < 44, 7	7.3 < <b>12.8</b> < 20.7, 5.9
	HIPA	X	72.6 < <b>74.4</b> < 76.3, 1.5	76.0 < <b>77.1</b> < 79.0, 1.3	76 < <b>89</b> < 100, 10	24.4 < <b>32.1</b> < 39.7, 10.8
		Z	71.5 < <b>73.7</b> < 77.2, 2.4	76.6 < <b>78.4</b> < 81.8, 2.2	40 < <b>63</b> < 78, 14	17.4 < <b>33.2</b> < 54.6, 16.6
7.2	AA	X	89.8 < <b>91.0</b> < 92.0, 0.8	90.7 < <b>91.4</b> < 91.9, 0.4	56 < <b>85</b> < 108, 17	34.0 < <b>39.8</b> < 49.7, 8.6
		Z	85.2 < <b>88.1</b> < 90.8, 2.1	89.5 < <b>92.1</b> < 95.5, 2.1	72 < <b>92</b> < 112, 13	21.4 < <b>35.8</b> < 41.5, 9.7
	HIPA	X	91.2 < <b>92.8</b> < 95.0, 1.5	89.6 < <b>91.1</b> < 92.7, 1.1	70 < <b>85</b> < 105, 14	32.9 < <b>43.5</b> < 48.8, 9.1
		Z	87.4 < <b>89.6</b> < 93.0, 1.9	92.3 < <b>93.0</b> < 94.0, 0.7	49 < <b>94</b> < 115, 23	28.3 < <b>34.3</b> < 46.7, 8.6

Results are presented as:  $\sigma_{min} < \bar{\sigma} < \sigma_{max}, SD$  where  $\sigma_{min}$  is the lowest value,  $\bar{\sigma}$  the mean value,  $\sigma_{max}$  the highest value and  $SD$  the standard deviation from the mean value.

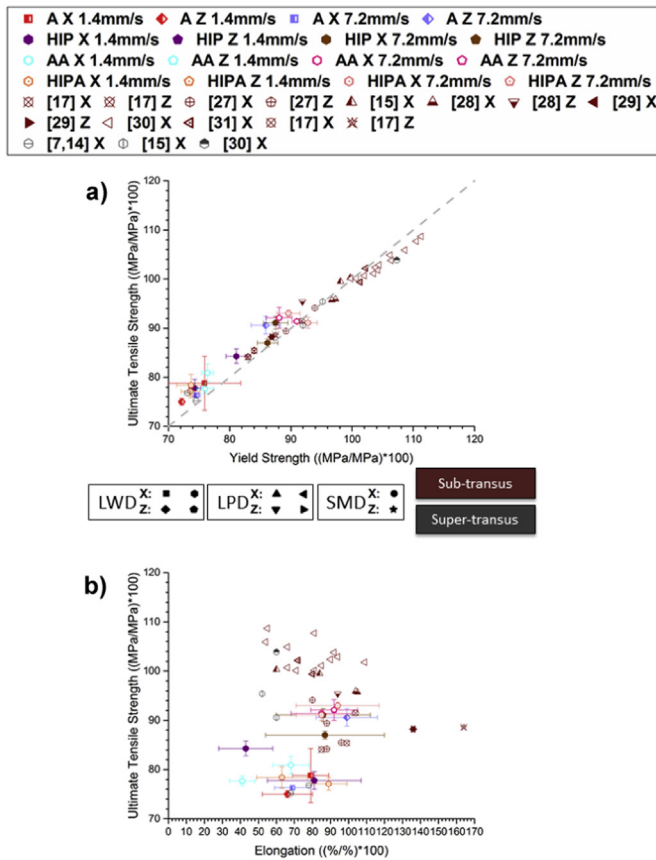


Fig. 2. Investigation of the reported static tensile properties along X or Z at room temperature comparing three different DED processes including LWD, LPD and SMD in the annealed or HIPed below the  $\beta$  transus temperature with or without aging in dark red and annealed or HIPed above the  $\beta$  transus temperature with or without aging in grey: a) Ultimate tensile strength versus yield strength and b) Ultimate tensile strength versus elongation. (For interpretation of the references to color in this figure legend, the reader is referred to the web version of this article.)

having similar  $L/A^{1/2}$  ratios. However, this is clearly not the case after reviewing the geometrical properties of the tested specimens within the investigated literature. These ratios can reach values as low as 3.2 [24], but also as high as 13.4 [32], with an average value of 7.3 [7,10,14,15,17,24,27,29,30,32–34]. This average value is closer to the ratio of 8.4 used for the post deposition heat-treated samples in this study. Sergueeva et al. [35] suggested to use a compliance correction factor in order to reduce the influence of the geometry on the final reported elongation. This requires though parameters proper to the tensile testing machine, which are most of the time not reported. Each of the processes reported are also characterized by unique thermal histories induced by the choice of deposition parameters and the repeated deposition of multiple beads. As a consequence, very different structural features can be developed within the deposits affecting in turn the elongation. It is believed however that aging cycles post deposition such as the stress relief cycle and the aging cycle would help in improving elongation by precipitating the  $\beta$  phase. A more even repartition of the  $\beta$  phase along the  $\alpha$  platelets boundaries increases the probability of dislocations to cross slip from the  $\alpha$  phase to the  $\beta$  phase and reciprocally. Indeed, typical slip systems activated in the  $\alpha$  phase during a deformation include the basal  $(0002)_\alpha[11\bar{2}0]_\alpha$  and prismatic  $(10\bar{1}0)_\alpha[11\bar{2}0]_\alpha$  slip systems [32,36]. A low stacking-fault energy associated with Ti-6Al-4V [32] combined with the knowledge of the burgers relationship [5] show that dislocations moving on these slip systems can be transmitted to the  $\beta$  phase through the  $(110)_\beta[1\bar{1}1]_\beta$  and  $(112)_\beta[1\bar{1}1]_\beta$  slip systems [36].

### 3.3. Fracture mechanisms

A summary of typical fracture surfaces regardless of experienced post deposition heat treatment or travel speed is shown in Fig. 3. Samples tested along the columnar prior  $\beta$  grains mainly exhibited a transgranular type of fracture as shown in Fig. 3a). In this case, crack propagation is mostly affected by the arrangement of alpha platelets yielding to a serrated crack profile as shown in Fig. 3c). Samples tested orthogonal to the columnar prior  $\beta$  grains were mainly characterized by a combination of intergranular and transgranular fracture modes as shown in Fig. 3b). A clear example of intergranular type of fracture is shown in Fig. 3d) occurring along a grain boundary allotriomorph  $\alpha_{GB}$  and associated to colonies of  $\alpha$  platelets all along. Overall, similar fracture behavior occurred when compared with the SR specimens [19].

In general, fractographs revealed a ductile type of fracture associated to the presence of dimples as shown in Fig. 3f). However, a higher density of smooth surfaces was observed for samples processed at 1.4 mm/s and as shown in Fig. 3e). These surfaces are believed to be generated by the presence of colonies of  $\alpha$  platelets [37,38], which is in agreement with the slower cooling rates experienced by the samples built in this condition [19]. The four sub- $\beta$  post deposition heat treatments were associated with an increased necking activity, regardless of travel speed as shown by the macrographs in Figs. 3e) and 3f) and also by the generated results in terms of reduction of area in Tables 4 and 5. This is in agreement with the measured higher elongations when compared to the SR condition [19].

### 3.4. Hardness

Table 6 summarizes all the hardness measurements developed in this study which produced statistically similar hardness results as in the AB condition [19]. Strengthening of titanium alloys and more specifically Ti-6Al-4V can be influenced by different structural properties [5,6,18,39] affecting in turn the measured hardness of the materials. Most important ones are strengthening induced by the material's dislocation density that can be measured by the amount of strain hardening, grain boundary strengthening, precipitation strengthening and solid solution strengthening by alloying elements and impurities. Each of which will be discussed in the following sections.

#### 3.4.1. Strain hardening

The Hollomon equation can be used to have a better qualitative description of the strain hardening and is defined as follow:

$$\sigma_T = K\varepsilon_T^n \quad (4)$$

Where  $\sigma_T$  is the true stress,  $K$  the strength coefficient,  $\varepsilon_T$  the true strain and  $n$  the strain-hardening exponent. This equation is valid from the onset of plastic deformation at the yield strength to the onset of necking starting at the ultimate tensile strength. Figs. 4 and 5 show experimental changes in the strain hardening coefficient  $n$  as a function of true strain  $\varepsilon_T$  for all the heat treated samples at both travel speeds including results generated for the SR condition [19]. In general, a higher strain hardening is observed for all conditions when tested along the Z direction with the exception of the annealed and aged condition processed at 1.4 mm/s. Onset of necking is also usually met faster for samples tested orthogonal to the columnar prior  $\beta$  grains. This suggests that in general a higher elongation would be met when tested along the columnar prior  $\beta$  grains which is in agreement with the average values provided in Tables 4 and 5.

Overall and whether samples were processed at 1.4 mm/s or 7.2 mm/s, all the heat treatments generated strain hardening results within the same range. However, a clear strengthening of the material occurred following a stress relief cycle as presented in a previous study [19]. Strain hardening seems in turn inadequate to account for that result.

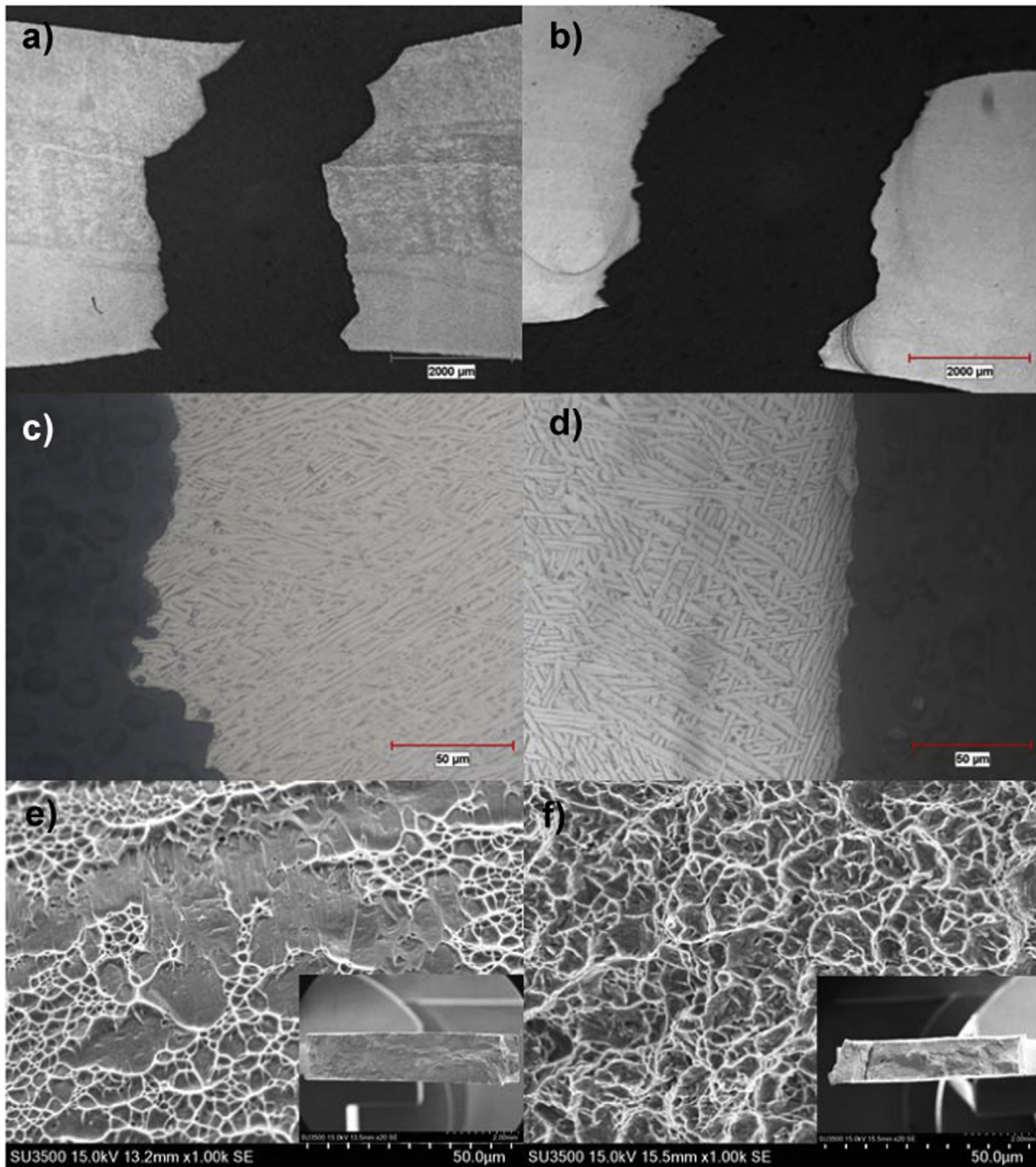


Fig. 3. Optical macrographs of fracture profiles processed at 7.2 mm/s a) in the HIPed and aged condition and tested in the Z direction and b) in the annealed and aged condition and tested in the X direction. Optical micrographs of fracture profiles in the HIPed and aged condition processed at 7.2 mm/s and tested in the X direction and d) in the annealed and aged condition processed at 1.4 mm/s and tested in the Z direction. SEM fractographs e) in the HIPed condition processed at 1.4 mm/s and tested in the X direction and f) in the annealed and aged condition processed at 7.2 mm/s and tested in the Z direction.

Table 6  
Developed Vickers microhardness.

Thermal Cycle	Travel Speed	
	1.4 mm/s	7.2 mm/s
A	307HV ± 17HV	330HV ± 18HV
HIP	302HV ± 17HV	314HV ± 18HV
AA	311HV ± 20HV	314HV ± 15HV
HIPA	316HV ± 15HV	322HV ± 26HV

3.4.2. Grain boundary strengthening

A Hall-Petch type of relationship as a function of the α lath thickness can be used to describe the effect of grain boundary strengthening

in Ti-6Al-4V lamellar structures [40–43]. A mathematical expression based on Eshelby's [44] work was proposed to quantify the relationship between the yield strength and the inverse square root of α platelets thicknesses as follow:

$$\sigma_{YS} = m_T(\tau_0 + k_S t_\alpha^{-1/2}) \tag{5}$$

Where  $\sigma_{YS}$  is the yield strength,  $m_T$  the Taylor factor,  $\tau_0$  the resolved shear stress of a single crystal,  $t_\alpha$  the α platelets thickness and  $k_S$  the Hall-Petch constant defined as:

$$k_S = \sqrt{4\tau_C G b / (q\pi)} \tag{6}$$

Where  $\tau_C$  is the critical shear strength,  $G$  the shear modulus,  $b$  the burger's slip length and  $q$  a constant that is equal to 0.67 for edge

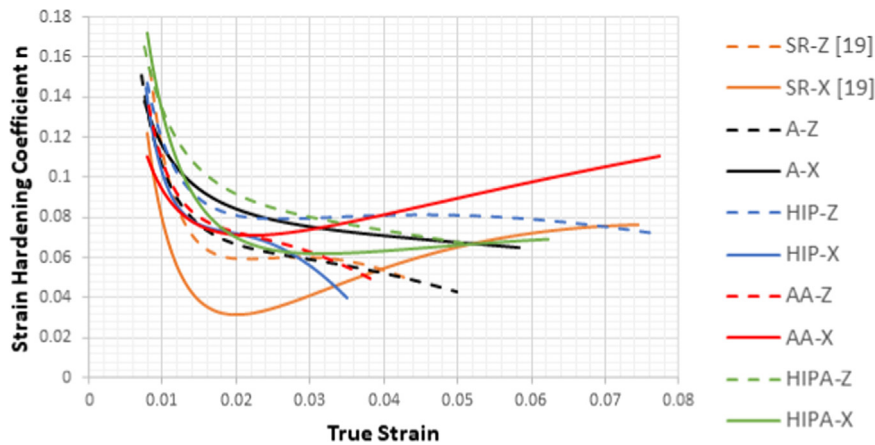


Fig. 4. Strain hardening exponent as a function of true strain derived for the samples processed at 1.4 mm/s in the X and Z directions and under all the heat-treated conditions. (For interpretation of the references to color in this figure legend, the reader is referred to the web version of this article.)

dislocations and 1 for screw dislocations.

Yield strength derived within this study for the two travel speeds in function of the inverse square root of  $\alpha$  platelets thickness is depicted in Fig. 6. Two linear regressions associated with the modified Hall-Petch relationship can be obtained in function of the selected travel speed. They both show good linear correlation coefficients of 93.5% and 91.6% for samples processed at 1.4 mm/s and 7.2 mm/s respectively. Derived equations are shown in Fig. 6 for both conditions. Assuming the Taylor factor equal to 3 [43,45,46],  $k_s$  can be determined experimentally as  $0.0101 \text{ MPa}\sqrt{\text{m}} \left(\frac{100}{\text{MPa}}\right)$  for samples processed at 1.4 mm/s and  $0.0054 \text{ MPa}\sqrt{\text{m}} \left(\frac{100}{\text{MPa}}\right)$  for samples processed at 7.2 mm/s and assuming the experimental values for  $G$  as 44.4 GPa for 1.4 mm/s or 47.2 GPa for 7.2 mm/s, the critical shear strength as  $0.01 G$  [43,46,47] and  $b = 3 \cdot 10^{-10} \text{ m}$  for  $\langle a \rangle$  slip [43,46,47]: computed  $k_s$ , normalized in terms of strength with the wrought minimum requirements for yield strength as set by the AMS4911 specification, provides  $0.0100 \text{ MPa}\sqrt{\text{m}} \left(\frac{100}{\text{MPa}}\right)$  for screw dislocations and  $0.0122 \text{ MPa}\sqrt{\text{m}} \left(\frac{100}{\text{MPa}}\right)$  for edge dislocations at 1.4 mm/s and  $0.0106 \text{ MPa}\sqrt{\text{m}} \left(\frac{100}{\text{MPa}}\right)$  for screw dislocations and  $0.0129 \text{ MPa}\sqrt{\text{m}} \left(\frac{100}{\text{MPa}}\right)$  for edge dislocations at 7.2 mm/s. These results show that the estimated Hall-Petch constants are closer to the one derived at 1.4 mm/s. This suggests that Eshelby's model is more appropriate in order to predict strength of samples that experienced slower cooling rates. The steeper slope of the linear regression associated to the samples produced at 1.4 mm/s also suggests that strength is more sensitive to slower travel speeds for almost similar  $\alpha$

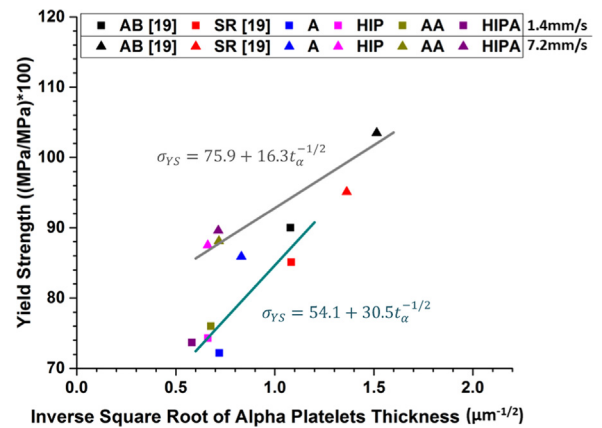


Fig. 6. Relationship between yield strength and the inverse square root of  $\alpha$  platelets thicknesses for samples processed at 1.4 mm/s and 7.2 mm/s.

platelets thicknesses.

Moreover, the increased number of boundaries for deposits processed at 7.2 mm/s would be aligned with a strengthening of the deposited material in the as-built condition. This is in agreement with the reported values in terms of strength [19] but can't effectively explain the statistically equivalent hardness developed at both travel speeds. The boundary strengthening mechanism in terms of  $\alpha$  platelets can't also be used to explain the higher hardness values induced by a stress

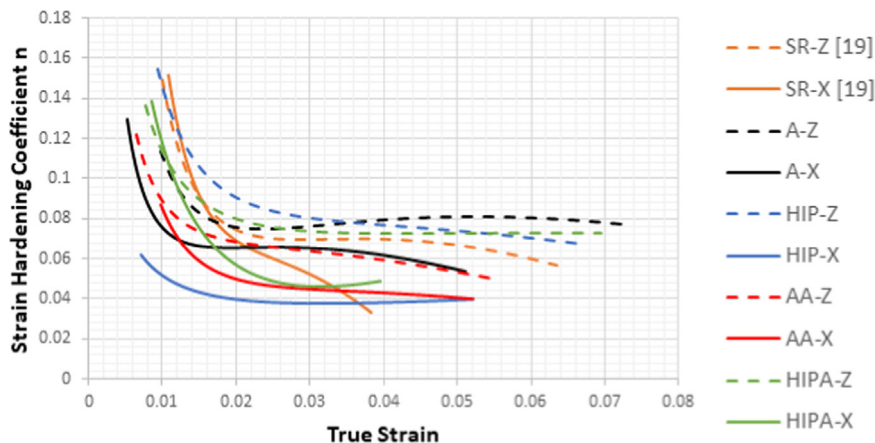


Fig. 5. Strain hardening exponent as a function of true strain derived for the samples processed at 7.2 mm/s in the X and Z directions and under all the heat-treated conditions. (For interpretation of the references to color in this figure legend, the reader is referred to the web version of this article.)

relief cycle when compared with the hardness values of the as-built condition for the respective travel speeds [19]. Finally, annealing or HIP, followed or not by aging, induced substantial coarsening of the  $\alpha$  platelets. All the values of  $\alpha$  platelets thicknesses were within the same range though, set at about 2  $\mu\text{m}$  and independent of the travel speed. This is in agreement with the similar hardness values reported in Table 6. However, grain boundary strengthening by itself does not explain the change in yield strength experienced by the two travel speed conditions and shown in Fig. 6.

These results suggest eventually that the travel speed dependent Hall-Petch type of relationship is not only affected by the  $\alpha$  platelet thickness with regards to strength values but also by their arrangements within the  $\beta$  matrix, which is not taken into account in Eq. (5). These arrangements are dictated by the overall experienced cooling rates [19].

#### 3.4.3. Precipitation strengthening

Some researchers suggested precipitation strengthening of  $\text{Ti}_3\text{Al}$  as a potential strengthening source following slow cooling rates [7,17]. Although, a closer look at a Ti-Al phase diagram shows that weight percentages of aluminum should exceed approximately 7.2% to precipitate  $\text{Ti}_3\text{Al}$  intermetallics at a temperature range close to the stress relief temperature. Reported aluminum concentrations both in  $\alpha$  and  $\beta$  phases hardly exceeded this threshold value [46,48]. And no concrete experimental data supports this hypothesis yet. Additionally, solvus temperature of  $\text{Ti}_3\text{Al}$  intermetallics is set at about 550 °C [14] which is below the stress relief temperature used in this study. Precipitation strengthening is not believed then to substantially affect hardness or yield strength values.

#### 3.4.4. Solid solution strengthening

Vickers hardness values and strength in the AB condition can be affected by solid solution strengthening mechanisms during the deposition process. Melt pool and heat affected zones increase the contamination risk of the alloy from the surrounding atmosphere especially through interstitial strengthening by oxygen. High levels of oxygen concentration within the deposit can undermine its mechanical properties. Yan et al. [49] have shown for instance that for oxygen levels exceeding 0.33% in weight percentage, elongation drops drastically and tends to 0%. It is then important to have a proper shielding of the deposition area in order to prevent the oxygen weight percentage within the deposits to exceed 0.20%. Since deposits were built in the same inert atmosphere with oxygen levels below 60ppmv, if interstitial strengthening by oxygen is still possible, a major difference in hardness induced by the change in travel speed between two deposits in the as-built condition should not be associated with it.

The difference in hardness in the SR condition [19] could originate from solid solution strengthening by diffusion of the main alloying elements. This would be in line with the observation of the precipitation of the  $\beta$  phase along the  $\alpha$  platelets boundaries as discussed in Section 3.1 but also in a previous study [19]. Brandl et al. [7] also suggested that solid solution strengthening by diffusion of the alloying elements was likely to happen following a stress relief by measuring aluminum and vanadium concentration through EDS line scans.

It was shown in the grain boundary strengthening section that an annealing or HIP heat treatment followed or not by aging, induced a softening of the material at both travel speeds. However, Table 6 showed that hardness values were equivalent to the hardness derived in the as-built condition [19]. As a consequence, a competing solid solution strengthening is still expected to happen as in the SR condition [19]. Hardness values would eventually remain fairly close to the measurements done in the as-built condition. Similar observations were also made in other studies [7,17,18].

## 4. Conclusion

Two different travel speeds and four different sub- $\beta$  transus post deposition heat treatments were investigated in this study in terms of structural development, subsequent tensile properties and strengthening mechanisms.

Even though an annealing or HIP post deposition heat treatments homogenized the microstructure by removing the macrostructural visual bands and producing statistically similar thicknesses in terms of alpha platelets, arrangement of alpha platelets within the prior  $\beta$  grains remained fairly similar. Substantially affecting in turn the generated tensile properties and stressing on the importance of selecting optimum deposition parameters at the start of the print. The additional aging thermal cycle was found to be critical in order to produce repeatable results. Samples produced at 7.2 mm/s produced in turn optimum isotropic tensile properties meeting or exceeding the minimum wrought requirements as set by AMS4911.

Results suggested as well that developed hardness was most likely affected by both solid solution strengthening and grain boundary strengthening. A major finding with regards to the grain boundary strengthening mechanism was its dependence to the selected travel speed suggesting again that the Hall-Petch type of relationship is not only affected by the thickness of  $\alpha$  platelets but also by their arrangements within the generated microstructure.

For future studies, further investigation on strengthening mechanisms will need to be done to better understand the solid solution strengthening mechanisms. Current effort by the authors is done in order to generate reliable quantitative EDS maps in an attempt to shed more light on these mechanisms. It will also be of interest to investigate the effects induced by a change in the deposited geometry by printing thicker specimens as real parts are rarely characterized by a constant wall thickness.

## Acknowledgments

The authors would like to thank the Consortium de Recherche et d'Innovation en Aérospatiale au Québec (CRIAQ), Liburdi, Centre de Métallurgie du Québec, Bell Helicopter Textron Canada, Bombardier, Edmit, GE, Héroux-Devtek, MDA and Pratt & Whitney Canada for their project contribution under the CRIAQ MANU-601/NSERC CRDPJ 451386-13 grants.

## References

- [1] C. Leyens, M. Peters, Titanium and Titanium Alloys. Fundamentals and Applications, Wiley-VCH, Weinheim, 2003.
- [2] F.H.S. Froes, M.N. Gungor, M.A. Imam, Cost-affordable titanium: the component fabrication perspective, JOM 59/6 (2007) 28–31.
- [3] I. Gibson, D.W. Rosen, B. Stucker, Additive Manufacturing Technologies Rapid Prototyping to Direct Digital Manufacturing, Springer, New York, 2010.
- [4] C.K. Chua, K.F. Leong, 3D Printing and Additive Manufacturing Principles and Applications, 4th edition, World Scientific, Singapore, 2014.
- [5] G. Lütjering, J.C. Williams, Titanium, Second edition, Springer, New York, 2007.
- [6] E. Brandl, V. Michailov, B. Viehweger, C. Leyens, Deposition of Ti-6Al-4V using laser and wire, Part I: Microstructural properties of single beds, Surf. Coat. Technol. 206 (2011) 1120–1129.
- [7] E. Brandl, A. Schoberth, C. Leyens, Morphology, microstructure, and hardness of titanium (Ti-6Al-4V) blocks deposited by wire-feed additive layer manufacturing (ALM), Mater. Sci. Eng. A532 (2012) 295–307.
- [8] J. Yu, M. Rombouts, G. Maes, F. Motmans, Material properties of Ti6Al4V parts produced by laser metal deposition, Phys. Procedia 39 (2012) 416–424.
- [9] N. Shamsaei, A. Yadollahi, L. Bian, S.M. Thompson, An overview of direct laser deposition for additive manufacturing; Part II: mechanical behavior, process parameter optimization and control, Addit. Manuf. 8 (2015) 12–35.
- [10] B. Baufeld, Effect of deposition parameters on mechanical properties of shaped metal deposition parts, J. Eng. Manuf. 226 (2011) 126–136.
- [11] T. Wang, Y.Y. Zhu, S.Q. Zhang, H.B. Tang, H.M. Wang, Grain morphology evolution behavior of titanium alloy components during laser melting deposition additive manufacturing, J. Alloy. Compd. 632 (2015) 505–513.
- [12] E. Brandl, V. Michailov, B. Viehweger, C. Leyens, Deposition of Ti-6Al-4V using laser and wire, Part II: hardness and dimensions of single beds, Surf. Coat. Technol. 206 (2011) 1130–1141.

- [13] S.M. Thompson, L. Bian, N. Shamsaei, A. Yadollahi, An overview of direct laser deposition for additive manufacturing; Part I: transport phenomena, modeling and diagnostics, *Addit. Manuf.* 8 (2015) 36–62.
- [14] E. Brandl, F. Palm, V. Michailov, B. Viehweger, C. Leyens, Mechanical properties of additive manufactured titanium (Ti-6Al-4V) blocks deposited by a solid-state laser and wire, *Mater. Des.* 32 (2011) 4665–4675.
- [15] G.P. Dinda, L. Song, J. Mazumder, Fabrication of Ti-6Al-4V scaffolds by direct metal deposition, *Metall. Mater. Trans.* 39A (2008) 2914–2922.
- [16] E. Brandl, D. Greitemeier, Microstructure of additive layer manufactured Ti-6Al-4V after exceptional post heat treatments, *Mater. Lett.* 81 (2012) 84–87.
- [17] E. Brandl, B. Baufeld, C. Leyens, R. Gault, Additive Manufactured Ti-6Al-4V using welding wire: comparison of laser and arc beam deposition and evaluation with respect to aerospace material specifications, *Phys. Procedia* 5 (2010) 595–606.
- [18] B. Baufeld, E. Brandl, O. van der Biest, Wire based additive layer manufacturing: comparison of microstructure and mechanical properties of Ti-6Al-4V components fabricated by laser-beam deposition and shaped metal deposition, *J. Mater. Process. Technol.* 211 (2011) 1146–1158.
- [19] N. Chekir, Y. Tian, R. Gauvin, N. Brodusch, J.J. Sixsmith, M. Brochu, Effect of Travel Speed and Stress Relief on Thin Ti-6Al-4V Laser Wire Deposits.
- [20] N. Stefansson, S.L. Semiatin, D. Eylon, The kinetics of static globularization of Ti-6Al-4V, *Metall. Mater. Trans.* 33A (2002) 3527–3534.
- [21] N. Stefansson, S.L. Semiatin, Mechanisms of globularization of Ti-6Al-4V during static heat treatment, *Metall. Mater. Trans.* 34A (2003) 691–698.
- [22] S.L. Semiatin, B.C. Kirby, G.A. Salishchev, Coarsening behavior of an alpha-beta titanium alloy, *Metall. Mater. Trans.* 35A (2004) (2809-281).
- [23] G. Lütjering, Influence of processing on microstructure and mechanical properties of ( $\alpha + \beta$ ) titanium alloys, *Mater. Sci. Eng.* A243 (1998) 32–45.
- [24] B.E. Carroll, T.A. Palmer, A.M. Beese, Anisotropic tensile behavior of Ti-6Al-4V components fabricated with directed energy deposition additive manufacturing, *Acta Mater.* 87 (2015) 309–320.
- [25] J.S. Keist, T.A. Palmer, Role of geometry on properties of additively manufactured Ti-6Al-4V structures fabricated using laser based directed energy deposition, *Mater. Des.* 106 (2016) 482–494.
- [26] P. Åkerfeldt, M.-L. Antti, R. Pederson, Influence of microstructure on mechanical properties of laser metal wire-deposited Ti-6Al-4V, *Mater. Sci. Eng. A* 674 (2016) 428–437.
- [27] E. Brandl, C. Leyens, C.D. Donne, et al., Deposition of Ti-6Al-4V using Nd:YAG laser & Wire: microstructure and mechanical properties, NATO AVT-163 Specialists Meeting on Additive Technology For Repair of Military Hardware, Bonn, Germany, 2009.
- [28] P.A. Kobryn, S.L. Semiatin, Mechanical Properties of Laser-Deposited Ti-6Al-4V, AFRL/MLLMP 179-186.
- [29] C. Qiu, G.A. Ravi, C. Dance, A. Ranson, S. Dilworth, M.M. Attallah, Fabrication of large Ti-6Al-4V structures by direct laser deposition, *J. Alloy. Compd.* 629 (2015) 351–361.
- [30] S. Zhang, X. Lin, J. Chen, W. Huang, Heat-treated microstructure and mechanical properties of laser solid forming Ti-6Al-4V alloy, *Rare Met.* 20/6 (2009) 537–544.
- [31] Y. Zhai, H. Galarraga, D.A. Lados, Microstructure, static properties, and fatigue crack growth mechanisms in Ti-6Al-4V fabricated by additive manufacturing: LENS and EBM, *Eng. Fail. Anal.* 69 (2016) 3–14.
- [32] F. Wang, S. Williams, P. Colegrove, A.A. Antonysamy, Microstructure and mechanical properties of wire and arc additive manufactured Ti-6Al-4V, *Metall. Mater. Trans.* 44A (2012) 968–977.
- [33] S.H. Mok, G. Bi, J. Folkes, I. Pashby, J. Segal, Deposition of Ti-6Al-4V using a high power diode laser and wire, Part II: investigation on the mechanical properties, *Surf. Coat. Technol.* 202 (2008) 4613–4619.
- [34] J. Alcisto, A. Enriquez, H. Garcia, S. Hinkson, T. Steelman, E. Silverman, P. Valdovino, H. Gigerenzer, J. Foyos, J. Ogren, J. Dorey, K. Karg, T. McDonald, O.S. Es-Said, Tensile properties and microstructures of laser-formed Ti-6Al-4V, *J. Mater. Eng. Perform.* 20/2 (2011) 203–212.
- [35] A.V. Sergueeva, J. Zhou, B.E. Meacham, D.J. Branagan, Gage length and sample size effect on measured properties during tensile testing, *Mater. Sci. Eng. A* 526 (2009) 79–83.
- [36] M. Simonelli, Y.Y. Tse, C. Tuck, Effect of the build orientation on the mechanical properties and fracture modes of SLM Ti-6Al-4V, *Mater. Sci. Eng.* A616 (2014) 1–11.
- [37] H.K. Rafi, N.V. Karthik, H. Gong, T.L. Starr, B.E. Stucker, Microstructures and mechanical properties of Ti6Al4V parts fabricated by selective laser melting and electron beam melting, *J. Mater. Eng. Perform.* 22/12 (2013) 3872–3883.
- [38] C. Buirette, J. Huez, N. Gey, A. Vassel, E. Andrieu, Study of crack propagation mechanisms during Charpy impact toughness tests on both equiaxed and lamellar microstructures of Ti-6Al-4V titanium alloy, *Mater. Sci. Eng. A* 618 (2014) 546–557.
- [39] J.J. Gilman, *Chemistry and Physics of Mechanical Hardness*, Wiley-Interscience, Hoboken, New Jersey, 2009.
- [40] J.J. Lin, Y.H. Lv, Y.X. Liu, B.S. Xu, Z. Sun, Z.G. Li, Y.X. Wu, Microstructural evolution and mechanical properties of Ti-6Al-4V wall deposited by pulsed plasma arc additive manufacturing, *Mater. Des.* 102 (2016) 30–40.
- [41] D.-G. Lee, S. Lee, C.S. Lee, S. Hur, Effects of microstructural factors on Quasi-static and dynamic deformation behaviors of Ti-6Al-4V alloys with Widmanstätten structures, *Metall. Mater. Trans.* A34 (2003) 2541–2548.
- [42] I. Sen, S. Tamirisakandala, D.B. Miracle, U. Ramamurty, Microstructural effects on the mechanical behavior of B-modified Ti-6Al-4V alloys, *Acta Mater.* 55 (2007) 4983–4993.
- [43] S.L. Semiatin, T.R. Bieler, The effect of alpha platelet thickness on plastic flow during hot working of Ti-6Al-4V with a transformed microstructure, *Acta Mater.* 49 (2001) 3565–3573.
- [44] J.D. Eshelby, The distribution of dislocations in an elliptical glide zone, *Phys. Status Solidi* 3/11 (1963) 2057–2060.
- [45] S.L. Semiatin, T.R. Bieler, Effect of texture and slip mode on the anisotropy of plastic flow and flow softening during hot working of Ti-6Al-4V, *Metall. Mater. Trans.* A32 (2001) 1787–1799.
- [46] X. Tan, Y. Kok, Y.J. Tan, M. Descoins, D. Mangelinck, S.B. Tor, K.F. Leong, C.K. Chua, Graded microstructure and mechanical properties of additive manufactured Ti-6Al-4V via electron beam melting, *Acta Mater.* 97 (2015) 1–16.
- [47] R.W. Armstrong, Engineering science aspects of the Hall-Petch relation, *Acta Mech.* 225 (2014) 1013–1028.
- [48] S.M. Kelly, S.L. Kampe, Microstructural evolution in laser-deposited multilayer Ti-6Al-4V builds: Part I. Microstructural characterization, *Metall. Mater. Trans.* 35A (2004) 1861–1867.
- [49] M. Yan, W. Xu, M.S. Dargusch, H.P. Tang, M. Brandt, M. Qian, Review of effect of oxygen on room temperature ductility of titanium and titanium alloys, *Powder Metall.* 57/4 (2014) 251–257.